

## **Supporting Information for** **Engineering Spin Coherence in Core-Shell Diamond Nanocrystals**

Uri Zvi, Denis R. Candido, Adam Weiss, Aidan R. Jones, Lingjie Chen, Iryna Golovina, Xiaofei Yu, Stella Wang, Dmitri V. Talapin, Michael E. Flatté, Aaron P. Esser-Kahn<sup>1</sup>, Peter C. Maurer\*

\*Peter C. Maurer

**Email:** pmaurer@uchicago.edu

### **This PDF file includes:**

Supporting Information text S11 to S10  
Figures S1 to S11  
SI References

### **Other supporting materials for this manuscript include the following:**

Dataset S1: RAW confocal and TEM images with the extracted sizes and photoluminescence counts of bare and core-shell particles used to produce Figure 1B

Dataset S2: T1 and T2 CPMG data set

## Supporting Information Text

### 1. Growth of silica shell on diamond nanocrystals

The growth of Silica shells on diamond nanocrystals (DN) was performed using a sol-gel Stöber process (1) from a tetraethyl orthosilicate (TEOS) precursor. To ensure uniform shell growth and prevent aggregation we had to improve the colloidal stability of the nanoparticles in the increasing ionic strength caused by the TEOS molecules. We modified a previously described (2) Polyvinylpyrrolidone (PVP) based technique that was also adapted for DNs (3). Briefly, 1 mg/mL of as purchased carboxylated DNs were sonicated for 20 min. In the meantime, 8 mg PVP (10 KDa; Sigma-Aldrich) was dissolved in 16.5 mL reversed-osmosis purified H<sub>2</sub>O (MQ-H<sub>2</sub>O) and sonicated for 10 min. The nanocrystals were added into the PVP solution and stirred at ~600 rpm overnight. The synthesized PVP-DNs were centrifuged at 20000Xg for 30 min, and the particles were redissolved by sonicated in 3.75 mL ethanol for 20 min (at this point the solution could be stored in 4C for further use). The solution was stirred and 10 µL of TEOS (Sigma-Aldrich) was added, followed by 42 µL of 30% ammonia. The solution was left to stir overnight after which it was purified by centrifugation for 15 min at 15000Xg and washed twice (10 min at 15000Xg) and finally suspended with 1 mL ethanol. For long-term storage, the solution was placed in Acetone instead. See Fig. S2-3 for illustration and chemical characterization of the synthesis process.

### 2. Preparation of TEM grids

To properly address single particles, we had to prevent aggregations. The low affinity to the substrate and the high surface to volume ratio cause the particles to agglomerate upon deposition. To increase the affinity to the substrate, the grids were treated with UV-ozone for 15 min creating a hydrophilic, negatively charged surface. The repulsion between the negative substrate and the negative particles' surface would still result in agglomeration (Fig. S4A, left panel). Therefore, for size analysis and PL measurements, 0.1 mg/mL of poly(ethyleneimine) (PEI; 2.5 KDa) in water was dropcasted on the treated grids for 2 min and wicked away. This process reversed the charge of the grids, affording much higher affinity to the nanocrystals (4). 0.05 mg/mL particles in water were placed on the positively charged grids for 2 min before the solution was wicked away. Grids treated this way present well dispersed particles (Fig. S4A, right panel). We noticed no effect of the PEI on the properties of the particles, but to ensure no influence, for coherence measurement we avoided using PEI. Instead, after UV-ozone treatment, a drop of particles was placed on the grids that were stored in a humid container on a rocker for 30 min after which the water was wicked away. This process allowed the particles to adsorb to the surface while minimizing agglomeration due to drying.

### 3. Size analysis

Size analysis for particles deposited on TEM grids was done using ImageJ, as described in the methods section. Equivalent diameter,  $D$ , was extracted using  $D = 2\sqrt{A/\pi}$ , where  $A$  is the area of the particles in the TEM image.

### 4. NV confocal set-up

NV measurements were performed using a home-built confocal microscope. Optical excitation was provided by a 520 nm pulsed laser (LABS electronics DLnsec) and focused onto the sample using a X60, NA=1.49 oil-immersion objective (Olympus APON60XOTIRFI). Translation of the excitation beam was done using a fast-steering mirror (Newport FSM-300). Epifluorescence emission was separated from the excitation beam using a dichroic filter (Chroma T610lpxr) and filtered (Semrock LP01-594R-25) before being focused onto a single-photon counting module (Excelitas, SPCM-ARQH-14).

## 5. EPR Measurements

The measurement procedure described in the methods section is sensitive to the total number of particles measured in each EPR experiment. Therefore, in order to properly compare results from bare and core-shell particles, the measurements had to be normalized to the number of particles. For normalization, we multiplied the EPR signal from core-shell particles by a normalization factor,  $F = N_{bare}/N_{CS}$ , where  $N_{bare}$  and  $N_{CS}$  are the number of bare and core-shell particles, respectively (Fig. S5). Since the average core diameter for the measured particles was ~70 nm (Fig. 3C) we used  $D_{DN} = 70$  nm DNs from adamas for our main EPR measurements. 1.04 mg of bare and 2.72 mg of core-shell lyophilized particles were transferred to EPR tubes for further measurements.

### **Analytical Normalization**

We calculated the volume weighted density of the core-shell particles,  $d_{CS} = (d_{DN} \times V_{DN} + d_{Si} \times V_{Si}) / (V_{DN} + V_{Si}) = 2.737 \text{ g/cm}^3$ , where  $d_{DN} = 3.3 \text{ g/cm}^3$ ,  $d_{Si} = 2.5 \text{ g/cm}^3$ , are the densities of DNs and amorphous silica, respectively, and  $V_{DN} = (4\pi/3) \times (D_{DN}/2)^3$ , and  $V_{Si} = V_{total} - V_{DN}$  are the per particle volume of the diamond core and the silica shell, respectively (we used 105 nm as the total diameter for core-shell particles). The mass and calculated density were used to extract  $F = N_{bare}/N_{CS} = 1.23$ .

### **Nanoparticle Tracking Analysis (NTA) Normalization**

Due to the possible loss while transferring particles in and out of the EPR tubes, the samples were measured again, confirming ~20% loss in mass for both bare and core-shell samples. 0.82 mg of bare and 2.25 mg of core-shell particles were dissolved in 0.82 mL and 1.25 mL MQ-H<sub>2</sub>O, respectively, for further analysis. 1  $\mu$ L was diluted (X10,000 for bare and X5,000 for core-shell) before 1 mL was injected to the Nanosight (Malvern Panalytical) instrument for particle count using the NTA 3.3 Dev Build 3.3.104 particle tracking software. The particles counted and the dilution factors were used to calculate  $F = N_{bare}/N_{CS} = 2.5$ .

### **Mass Etching Normalization**

250  $\mu$ L of 1 M KOH was added and the solution was shaken for 12 hrs to facilitate the etching of the entire silica shell. The solution was then washed thoroughly with 3 cycles of precipitation by centrifugation (20,000 g for 30 min), removal of the supernatant, and resuspension in MQ-H<sub>2</sub>O. The particles were then precipitated once more and were left to dry on a hot plate (90°C for 30 min) after supernatant removal. Finally, the mass of the dry sample was remeasured. The bare particles were processed in a similar manner to confirm negligible loss and negligible etching of the diamond core (Fig. S5A). The remaining mass (0.78 mg for bare and 0.57 mg for core-shell particles) was used to calculate  $F = N_{bare}/N_{CS} = 1.36$ .

### **Fitting**

The averaged normalization factor was used to normalize the core-shell to the bare EPR signal before the data was fitted to produce  $g = 2.0031 \pm 0.00005$  (see methods for fitting procedure). The data was deconvolved to extract parameters for X ( $g = 2.0032$ , and linewidth,  $\Delta B = 0.3 \text{ mT}$ ), P1 ( $g = 2.0026$ ,  $\Delta B = 0.3 \text{ mT}$ , hyperfine coupling,  $A_x = A_y = 82 \text{ MHz}$ ,  $A_z = 114 \text{ MHz}$ , and nuclear quadrupole coupling,  $P_z = -4 \text{ MHz}$ ), and H1 ( $g = 2.0028$ ,  $\Delta B = 0.65 \text{ mT}$ , and hyperfine coupling,  $A_x = A_y = 27.5 \text{ MHz}$ ,  $A_z = -5.5 \text{ MHz}$ ) paramagnetic centers with  $S = 1/2$  spin. The reduction factor of area under the curve of core-shell vs bare EPR signal was calculated to be 3.81, 2.56, and 1.8 for X, P1, and H1 centers, respectively (Fig. 2B).

## 40 nm Sample

A similar procedure was repeated with 40 nm particles (0.81 mg bare and 3.51 mg core-shell particles). Analytical ( $F = 0.98$ ) and mass etching ( $F = 0.83$ ) normalization was used to produce the data shown in Fig. S5B. P1 signal was undetectable in the 40 nm samples and instead featured a very low signature of an unknown center. The parameters for the bare sample: X ( $g = 2.0031$ ,  $\Delta B = 0.35$  mT), H1 ( $g = 2.0031$ ,  $\Delta B = 0.55$  mT) and unknown ( $g = 2.0032$ ,  $\Delta B = 2$  mT) paramagnetic centers. The parameters for the core-shell sample: X ( $g = 2.0031$ ,  $\Delta B = 0.4$  mT), H1 ( $g = 2.0031$ ,  $\Delta B = 0.4$  mT) and unknown ( $g = 2.0032$ ,  $\Delta B = 2$  mT) paramagnetic centers. The reduction factor of area under the curve of core-shell vs bare EPR signal was calculated to be 1.2, 2.6, and 0.8 for X, H1, and the unknown center, respectively. We attribute the smaller change to the probable different band structure for very small bare DNs, which might result in depopulation of P1 and NVs, (as supported by the inability to measure P1 signal).

## 6. Band Bending

### Alignment

Alignment details are provided in the method section. We didn't find exact values for our system (type 1b HPHT carboxylated DNs with ~70 ppm N impurities), but instead assessed them from literature values for similar systems, as described in the methods. The major guidelines were the ~2 eV electron affinity and downward band bending that has been previously measured in similar systems (5, 6). We note that all values were assessed strictly from literature and motivated, but weren't influenced by the band bending simulation we constructed. For clarity, Figure S6 shows the electronic structures used for our carboxylated DNs, the amorphous silica shell, and the heterojunction with the suggested bending effect.

### Simulation

Here we present our approach to calculate the band bending of both bare and core-shell DNs. The band bending is caused by the spatial variation of the electrostatic potential,  $\phi$ , produced by the equilibrium charge profile within the diamond (7). Accordingly, to obtain  $\phi$  we solved the Poisson's equation  $\nabla^2 \phi = -\rho(\phi)/\epsilon\epsilon_0$ , where  $\epsilon$  is the diamond dielectric constant,  $\epsilon_0$  is the vacuum permittivity, and  $\rho(\phi)$  is the charge density arising from electrons, holes, and charged states of P1, vacancies and NV-centers, namely:

$$\rho(r, \phi) = -en_{ex}(r, \phi) + ep_{ex}(r, \phi) + eN_D(r, \phi) - eN_{NV^-}(r, \phi) + eN_{NV^+}(r, \phi) - eN_{V^-}(r, \phi) + eN_{V^+}(r, \phi),$$

where  $n_{ex}$  and  $p_{ex}$  are the electron and hole densities, respectively,  $N_D$  is the density of ionized nitrogen donors,  $N_{NV^-}$  and  $N_{NV^+}$  are the densities of the charged NVs states, and  $N_{V^-}$  and  $N_{V^+}$  are densities of the charged vacancy states. They are given respectively by:

$$n_{ex}(r, \phi) = (2/\sqrt{\pi}) \times N_C(T) \times F_{1/2}(r, \phi) \times (E_F - \epsilon_C + e\phi(r))/k_B T$$

$$p_{ex}(r, \phi) = (2/\sqrt{\pi}) \times P_v(T) \times F_{1/2}(r, \phi) \times (\epsilon_v - E_F - e\phi(r))/k_B T$$

$$N_D(r, \phi) = (1 - \chi)N_N / [\exp([E_F - \epsilon_N + e\phi(r)]/k_B T) + 1]$$

$$N_{NV^-}(r, \phi) = \chi N_N / [\exp([\epsilon_{NV^-/0} - E_F - e\phi(r)]/k_B T) + 1]$$

$$N_{NV^+}(r, \phi) = \chi N_N / [\exp([E_F - \epsilon_{NV^+/0} + e\phi(r)]/k_B T) + 1]$$

$$N_{V^-}(r, \phi) = N_V / [\exp([\epsilon_{V^-/0} - E_F - e\phi(r)]/k_B T) + 1]$$

$$N_{V^+}(r, \phi) = N_V / [\exp([E_F - \epsilon_{V^+/0} + e\phi(r)]/k_B T) + 1]$$

where  $e > 0$  is the elementary charge,  $F_v(\delta) = \int_0^\infty x^v / [\exp(x - \delta) + 1] dx$  is the Fermi-Dirac integral,  $E_F$  is the Fermi level,  $k_B$  is the Boltzmann constant,  $T$  is the temperature,  $N_N$  is the density of implanted Nitrogen,  $\chi$  is the conversion of Nitrogen to NV centers, and  $N_V$  is the density of vacancies.  $\epsilon_C$  and  $\epsilon_v$  are

the bottom of the conduction and top of the valance bands, respectively,  $\varepsilon_N$  is the formation energy of Nitrogen donors.  $\varepsilon_{NV^-/0}$  and  $\varepsilon_{NV^+/0}$  are the formation energy associated with the  $NV^- \leftrightarrow NV^0$  and  $NV^+ \leftrightarrow NV^0$  transitions, respectively, and  $\varepsilon_{V^-/0}$  and  $\varepsilon_{V^+/0}$  are the formation energy associated with the  $V^- \leftrightarrow V^0$  and  $V^+ \leftrightarrow V^0$  transitions, respectively. Additionally, we have  $N_C(T) = (1/4)[2m_c k_B T / (\pi \hbar^2)]^{3/2}$  and  $P_v(T) = (1/4)[2m_v k_B T / (\pi \hbar^2)]^{3/2}$ , where  $\hbar$  is the reduced Planck's constant, and  $m_c$  and  $m_v$  are the effective electron and hole masses, respectively.

The solution for the corresponding Poisson's equation depends on the boundary conditions for  $\phi$ , in addition to the Fermi level,  $E_F$ . The latter is obtained by assuming neutral nanocrystals deep in the interior ( $r \approx 0$ ), where we assume  $\phi = 0$ . Accordingly, the value for  $E_F$  is obtained by imposing  $\rho(r = 0, \phi = 0) = 0$ . The other boundary condition, namely  $\phi(r = R) = \phi_S$ , defines the band bending at the diamond surface,  $r = R$  as obtained from the band alignment in Fig. 2C. Here we assume spherical nanocrystals with radius  $R$ . For both bare and core-shell particles, we have used  $m_e = 0.57m_0$  and  $m_h = 0.8m_0$  with electron bare mass  $m_0$ . Other parameters used:  $E_g = 5.45$  eV as the diamond band-gap,  $\varepsilon_N = 3.75$  eV,  $\varepsilon_{NV^0/-} = 2.85$  eV,  $\varepsilon_{NV^+/0} = 1.05$  eV,  $\varepsilon_{V^-/0} = 2.1$  eV,  $\varepsilon_{V^+/0} = 0.95$  eV (8, 9),  $\epsilon = 5.8$ ,  $T = 300$  K,  $N_D = 70$  ppm ( $15.6 \times 10^{18} \text{ cm}^{-3}$ ),  $\chi = 0.01$ , and  $N_V = 20$  ppm ( $2.8 \times 10^{18} \text{ cm}^{-3}$ ) (10, 11). With these values, we obtain  $E_F = 3.77$  eV for both bare and core-shell DN's. The surface electrostatic potential,  $\phi_S$ , was set to 0.5 eV and -0.225 eV for bare and core-shell particles, respectively, as obtained from the band alignment model in Fig. 2C. This includes the assumption that the amorphous silica shell has a similar defects density to the diamond. In short, the upward band bending present in core-shell DN's (near to the surface) is responsible for shifting the P1 formation energy above the Fermi level. As a consequence, we observe a corresponding depletion of P1. Our calculation indicates a 44% reduction, which is consistent with the 45% reduction seen in our EPR measurements (Fig. 2B). The results of the simulation are shown in Figure S7.

## 7. DEER

After EPR measurements demonstrated the reduction of paramagnetic species in core-shell particles, we aimed to confirm the coupling of these paramagnetic species to the NVs in our particles. The DEER protocol, described in reference (12) and shown in Fig S8, normalizes the contrast of the DEER decay with respect to Hahn echo decay to remove the effect from other noise sources. To measure the resonance frequencies of the paramagnetic defects, we keep the spacing between pulses constant (the spacing between  $\pi$  pulse and  $\pi/2$  pulse was fixed at 200 ns) and sweep the microwave frequency. To isolate the coupling from the paramagnetic defects, we modify the DEER sequence by keeping the microwave at the main paramagnetic defects resonance frequency and sweeping the duration between pulses. The normalized time trace signal (DEER decay normalized with respect to Hahn echo decay) is equivalent to free induction decay of the NV center caused by the paramagnetic defects alone (13). Hence, by comparing the decay rate (dephasing rate) of the normalized signal, we can compare the average paramagnetic defects coupling before and after core-shell coating. The Hahn echo decay was fitted with:

$$C_{Echo}(\tau) = \exp[-(\tau/T_2)^{N_E}].$$

The regular DEER decay part was fitted using:

$$C_{DEER}(\tau) = \exp[-(\tau/T_2)^{N_E} - (\tau/T_{FID})^{N_{FID}}].$$

Where  $T_2$  and  $N_E$  were fitted values determined from the Hahn echo decay, the extra decay terms  $T_{FID}$  and  $N_{FID}$  are therefore due to the paramagnetic defects alone.

DEER resonances at ~0.498 GHz, ~0.591 GHz, and ~0.669 GHz validated the coupling to P1 (14) (all 3 resonances) and X-spins (contribute to central resonance). Core-shell particles showed suppressed

signal at  $\sim 0.498$  GHz and  $\sim 0.669$  GHz (Fig. S8B), confirming the significant reduction in P1 defects seen in EPR. We attribute the lack of reduction of the central frequency to the increased relaxation times of the surface spins that compensates for the total reduction in density. We resonantly drive the central frequency of the splitting and perform correlation measurements (lower sequence in Fig. S8A) to find a Rabi frequency for the paramagnetic defects of 12.8 MHz (Fig. S8C). DEER FID was measured to compare the contribution of paramagnetic defects to NV decoherence in bare and core-shell particles. As seen in Figure S8D-F, core-shell particles presented longer DEER FID times (0.91  $\mu$ s and 0.99  $\mu$ s) compared to DEER FID times of the bare particle (0.78  $\mu$ s). This strongly supports the results presented in Fig. 2 and indicate a reduced density of P1 and X-spins in core-shell particles.

## 8. Relaxation Measurements

Setting  $\gamma$  as the DQ transition rate and  $\Omega$  as the SQ transition rate, the population dynamics of the NV triplet states can be represented by:

$$\rho_0(\tau) = \frac{1}{3} + \left( \rho_0(0) - \frac{1}{3} \right) e^{-3\Omega\tau},$$

$$\rho_{\pm 1}(\tau) = \frac{1}{3} \pm \frac{1}{2} \Delta\rho_{\pm 1}(0) e^{-(\Omega+2\gamma)\tau} - \frac{1}{2} \left( \rho_0(0) - \frac{1}{3} \right) e^{-3\Omega\tau}$$

where  $\tau$  is the time between initialization and readout,  $\rho_m$  are the states' populations with the condition  $\rho_{+1} = 1 - \rho_{-1} - \rho_0$ , and the initialization conditions determine  $\rho_0(0)$  and  $\Delta\rho_{\pm 1}(0)$ . We extract  $T_1^{SQ} = \frac{1}{3\Omega}$  and  $T_1^{DQ} = \frac{1}{\Omega+2\gamma}$ . We denote the initial,  $i$ , and measured,  $j$ , time-dependent populations as  $\rho_{i,j}(\tau)$  and fit the signal to:

$$F_{SQ}(\tau) = \rho_{0,0}(0) - \rho_{0,-1}(0) = a e^{-3\Omega\tau},$$

$$F_{DQ}(\tau) = \rho_{-1,-1}(0) - \rho_{-1,+1}(0) = a e^{-(\Omega+2\gamma)\tau},$$

where  $a$ , and  $T_1^{SQ}$  or  $T_1^{DQ}$  are the fit parameters.

## 9. $T_2$ Measurements

### *Dynamical Decoupling*

Theoretical treatment of the NV spin decoherence under CPMG dynamical decoupling is given in the Noise spectral density section of the methods and in SI11. After measuring the Hahn Echo decay times,  $T_2$  was measured with a choice of  $N = 8, 16, 32, 64, 128, 256, 512, 1024, 1472$  (or 1536) up to the point where no more improvement was seen, or no contrast was detected during the set measurement time. For most particles, following Hahn Echo measurements,  $T_2$  was measured with  $N = 512$ . If contrast was detected and a decay fit was obtained,  $T_2$  was measured for  $1024 \leq N \leq 1536$  to obtain the maximum  $T_2$  measured for a given particle. If a contrast was not detected,  $T_2$  was measured for  $N = 256$  and the process repeated until an  $N$  for which contrast was detected, which was considered the saturation point. All  $T_2$  measurements were collected  $\sim 1.5e6$  times.

### *Simulation for the Effect of Dephasing During $\pi$ -Pulses*

It is important to emphasize that the calculations concerning  $T_2$  decay signals, both in this work and in most other published work, consider  $\pi$ -pulses as delta functions. In reality, this is not the case, and the role of the  $\pi$ -pulses duration on the decoherence needs to be taken into account. Michael J. Biercuk et al (15) have tackled this by considering the absence of dephasing during the  $\pi$ -pulses. We stress that this relies exclusively on the assumption of a  $\pi$ -pulse length,  $t_\pi$ , much shorter than the correlation time of the random fluctuations,  $\tau_c$ , i.e.,  $t_\pi \ll \tau_c$ . For our system, however, we have  $t_\pi \approx 20$  ns and  $\tau_c \approx 1$  ns for bare or  $\tau_c \approx 50$  ns for core-shell particles. For these conditions, the formulas within reference (15) cannot be

employed. Accordingly, here we implemented Monte-Carlo simulations to assess completely the role of the dephasing during the application of  $N$  number  $\pi$ -pulse. Specifically, we simulate the dephasing of a spin qubit system during the CPGM pulse sequence, under the influence of a random field  $H/\hbar = \gamma S_{NV}^z B^z(t)$ . We choose a random Gaussian field with correlation function  $\langle B^z(t) B^z(0) \rangle = \langle \delta B^2 \rangle e^{-t/\tau_c}$ , standard deviation  $\langle \delta B^2 \rangle$ , and correlation time  $\tau_c$ . We first looked at the exact (derived in SI11) and the approximated ( $C(t) \approx \exp[-S(\omega_0)t]$ ) decay considering the  $\pi$ -pulse as a delta function ( $t_\pi = 0$  ns), with  $N = 10$ ,  $\tau_c = 1$  ns, and  $\gamma^2 \langle \delta B^2 \rangle = 1/400$  ns<sup>-2</sup>. We compared these with the exact and approximated solutions for  $t_\pi = 10$  ns. We show that for our experimental conditions of  $t_\pi > \tau_c$  and  $t > N t_\pi$ , the formula for the coherence,  $C(t) \approx \exp[-S(\omega_0)t]$  still holds. The results are summarized in Fig. S9B.

## 10. Noise Spectral Density

### Placing DQ, CPMG, and SQ on the Same Scale

We follow the procedure at Myers et al. (16) to compare DQ, CPMG, and SQ noise directly. Briefly, we represent each in terms of effective  $E_\perp$  electric field noise spectrum, using:

$$S_{E_\perp}^{SQ}(\omega) = 2S_{E_\parallel}^{SQ}(\omega) = 2 \frac{S_{SQ}(\omega)}{d_\parallel^2},$$

$$S_{E_\perp}^{DQ}(\omega) = \frac{S_{DQ}(\omega)}{d_\perp^2},$$

where  $S_{DQ}(\omega) = \gamma(\omega)$  and  $S_{SQ}(\omega) = \Omega(\omega)$  are obtained as described in the *T<sub>1</sub> measurements and fitting* section of the methods. The procedure to obtain  $S_{SQ}(\omega)$  for CPMG data is described in detail in the *Noise Spectral Density* section of the methods.

## 11. Coherence Exponent Analysis

The decoherence of our qubit is obtained by assuming our NV center interacting with a D-dimensional fluctuating spin bath via the Ising Hamiltonian:

$$H/\hbar = \sum_{j=1}^N C[S_j^z(t) S_{NV}^z / |r_j(t) - r_{NV}|^\alpha] = \gamma \sum_{j=1}^N B_j^z(t) S_{NV}^z,$$

where  $r_j$  is the position of the spin bath fluctuators,  $r_{NV}$  is the position of the NV-center, and  $C$  is the NV-bath interaction strength. In the presence of a dynamical decoupling sequence with equally spaced  $N$   $\pi$ -pulse, the coherence of a qubit initialized as  $|\psi(t=0)\rangle = (|0\rangle + e^{i\phi}|1\rangle)/\sqrt{2}$  is given by:

$$C(t) = \langle \exp[i\gamma \int_{-\infty}^{\infty} d\tau \lambda(\tau) \sum_j B_j^z(t)] \rangle, \quad (\text{eq. 3})$$

where  $\langle \rangle$  is the ensemble average, and the effect of spin echo:  $\lambda(\tau) = 1$  for  $0 \leq \tau \leq t/2$ ,  $\lambda(\tau) = -1$  for  $t/2 \leq \tau \leq t$  and  $\lambda(\tau) = 0$  for  $\tau > t$ ,  $\tau < 0$ , is taken into account. We now treat the decoherence under two different physical situations: fixed or changing spin-bath positions ( $r_j$ ).

### Fixed Position for the Spin Bath

For fixed bath positions, we can replace the sum of the fluctuating fields by a total fluctuating field,

$\sum_{j=1}^N B_j^z = \sum_{j=1}^N C[S_j^z(t)/|r_j(t) - r_{NV}|^\alpha]$ . Assuming a Gaussian character for our noise, i.e.,  $\langle e^{i\phi} \rangle = e^{-(\phi^2/2)}$ , we can rewrite the decoherence as:

$$C(t) = \exp[-\frac{1}{2} \gamma^2 \int_{-\infty}^{\infty} \int_{-\infty}^{\infty} d\tau d\tau' \lambda(\tau) \lambda(\tau') \langle B^z(\tau) B^z(\tau') \rangle] = \exp[-\chi(t)].$$

Accordingly,

$$\langle B^z(\tau)B^z(\tau') \rangle = C^2 \sum_{j,k} \langle S_j^z(\tau)S_k^z(\tau') \rangle / [|r_j - r_{NV}|^\alpha |r_j - r_{NV}|^\alpha] \approx C^2 \sum_j \langle S_j^z(\tau)S_k^z(\tau') \rangle / |r_j - r_{NV}|^{2\alpha}$$

assuming the correlation persists only between same spins, i.e.,  $\langle S_j^z(\tau)S_k^z(\tau') \rangle = \delta_{j,k} \langle S_j^z(\tau)S_k^z(\tau') \rangle$ . For large number of spin-bath fluctuators, we substitute the discrete sum by an integral,  $\sum_j 1/|r_j - r_{NV}|^{2\alpha} \rightarrow \int dr n/|r - r_{NV}|^{2\alpha}$ , where  $n$  is the constant density of fluctuators (16–20). This can also be written as an integral over the frequency space, namely:

$$\chi(t) = -\frac{1}{2} \int_{-\infty}^{\infty} \frac{d\omega}{2\pi} S(\omega) |\lambda(\omega, t)|^2,$$

with

$$S(\omega) = -\gamma^2 \int d\tau e^{i\omega\tau} \langle B^z(\tau)B^z(0) \rangle \propto \int d\tau e^{i\omega\tau} \langle S^z(\tau)S^z(0) \rangle$$

and filtering function (21, 22):

$$|\lambda(\omega, t)|^2 = \begin{cases} \tan^2[\omega t/(2(N+1))] [\cos^2(\omega t/2)/(\omega/2)^2], & N: \text{even} \\ \tan^2[\omega t/(2(N+1))] [\sin^2(\omega t/2)/(\omega/2)^2], & N: \text{odd} \end{cases}$$

For  $N \gg 1$ ,  $\lambda(\omega, t)$  presents a primary peak at  $\omega = \omega_0 = N\pi/t$ , yielding  $C(t) \approx \exp[-S(\omega_0)t]$ .

### Spin Echo

For  $N = 1$  and assuming correlation function of the form  $\langle B^z(\tau)B^z(\tau') \rangle = \langle \delta B^2 \rangle e^{-|\tau - \tau'|/\tau_c}$ , with correlation time  $\tau_c$  and standard deviation  $\sqrt{\langle \delta B^2 \rangle}$ , we obtain:

$$C(t) = \exp \{ [-\gamma^2 \langle \delta B^2 \rangle \tau_c [t - \tau_c (e^{-t/\tau_c} - 4e^{t/2\tau_c} + 3)]] \}$$

and

$$C(t) = \begin{cases} \exp [-\gamma^2 \langle \delta B^2 \rangle t^3 / 6\tau_c], & t \ll \tau_c \\ \exp [-\gamma^2 \langle \delta B^2 \rangle 2t\tau_c], & t \gg \tau_c \end{cases}$$

thus, showing an early and late slope (22).

$$\chi(t) \propto \begin{cases} t^3, & t \ll \tau_c \\ t, & t \gg \tau_c \end{cases}$$

### Configurational Averaging

In the derivation above, we have assumed that the position of the spin-bath fluctuators are fixed and do not change as a function of time. Although this could be accurate for some cases, reconfiguration of the spins during photoexcitation with green laser has been reported (13, 23). To take this phenomenon into account, we employ an average over the different position configurations following references (13, 23–27). We again start with the coherence equation (eq. 3). After assuming both Gaussian noise and  $\langle S_j^z(\tau)S_k^z(\tau') \rangle = \delta_{j,k} \langle S_j^z(\tau)S_k^z(\tau') \rangle$ , we obtain:

$$C(t) = \exp \left[ -\frac{1}{2} \gamma^2 \sum_{j=1}^N C^2 / |r_j - r_{NV}|^{2\alpha} \int_{-\infty}^{\infty} \int_{-\infty}^{\infty} d\tau d\tau' \lambda(\tau) \lambda(\tau') \langle S^z(\tau)S^z(\tau') \rangle \right]$$

Defining:

$$F(t) = \langle \left[ \int_{-\infty}^{\infty} d\tau \lambda(\tau) S^z(\tau) \right]^2 \rangle = \int_{-\infty}^{\infty} \int_{-\infty}^{\infty} d\tau d\tau' \lambda(\tau) \lambda(\tau') \langle S^z(\tau)S^z(\tau') \rangle$$

we obtain:

$$C(t) = \prod_{j=1}^N \exp \left[ -\frac{1}{2} (\gamma C)^2 F(t) / |r_j - r_{NV}|^{2\alpha} \right].$$



Averaging over different positional configurations and assuming the N-spin bath fluctuators in a D-dimension volume ( $L^D$ ),

$$\begin{aligned}
C(t) &= \int \dots \int \left( \frac{d^D \underline{r}_1}{L^D} \right) \left( \frac{d^D \underline{r}_2}{L^D} \right) \dots \left( \frac{d^D \underline{r}_N}{L^D} \right) \prod_{j=1}^N \exp \left[ -\frac{1}{2} (\gamma C)^2 F(t) / |\underline{r}_j - \underline{r}_{NV}|^{2\alpha} \right] \\
&= \int \dots \int \left( \frac{d^D \underline{r}_1}{L^D} \right) \exp \left[ -\frac{1}{2} (\gamma C)^2 F(t) / |\underline{r}_{NV} - \underline{r}_1|^{2\alpha} \right] \dots \left( \frac{d^D \underline{r}_N}{L^D} \right) \exp \left[ -\frac{1}{2} (\gamma C)^2 F(t) / |\underline{r}_{NV} - \underline{r}_N|^{2\alpha} \right] \\
&= \left\{ \int (d^D \underline{r} / L^D) \exp \left[ -\frac{1}{2} (\gamma C)^2 F(t) / |\underline{r}_{NV} - \underline{r}|^{2\alpha} \right] \right\}^N \\
&= \left\{ 1 - \frac{1}{L^D} \int d^D \underline{r} \{ 1 - \exp \left[ -\frac{1}{2} (\gamma C)^2 F(t) / |\underline{r}_{NV} - \underline{r}|^{2\alpha} \right] \} \right\}^N
\end{aligned}$$

Using now  $\exp(-x) = \lim_{M \rightarrow \infty} (1 - x/M)^M$  where the fluctuator density is  $n = N/L^D$  with  $L^D \rightarrow \infty$  (thermodynamic limit), we obtain:

$$C(t) = \exp \left[ -n \int d^D \underline{r} \{ 1 - \exp \left[ -\frac{1}{2} (\gamma C)^2 F(t) / |\underline{r}_{NV} - \underline{r}|^{2\alpha} \right] \} \right].$$

We now assume a D-hypersphere of fluctuations and  $\underline{r}_{NV} = 0$ , so our integral becomes:

$$\int d^D \underline{r} \{ 1 - \exp \left[ -\frac{1}{2} (\gamma C)^2 F(t) / r^{2\alpha} \right] \} = \int d\Omega \int dr r^{D-1} \{ 1 - \exp \left[ -\frac{1}{2} (\gamma C)^2 F(t) / r^{2\alpha} \right] \}$$

Defining  $x = \gamma C \sqrt{F(t)} / r^\alpha$ , we get:

$$\frac{1}{\alpha} \int d\Omega [\gamma C \sqrt{F(t)}]^{D/\alpha} \int_{x1}^{\infty} dx (1 - \exp \left[ -\frac{1}{2} x^2 \right]) / x^{(D+\alpha)/\alpha},$$

with  $x1 = \frac{\gamma C \sqrt{F(t)}}{R}$ . For  $x1 \rightarrow 0$ , the integral only converges for  $D/\alpha < 2$ ,

$$\int_{x1}^{\infty} dx (1 - \exp \left[ -\frac{1}{2} x^2 \right]) / x^{(D+\alpha)/\alpha} = 2^{-(D+2\alpha)/2\alpha} \Gamma(-D/2\alpha)$$

and finally:

$$C(t) = \exp \left[ -\{n/(\alpha 2^{(D+2\alpha)/2\alpha})\} \Gamma(-D/2\alpha) \int d\Omega (\gamma C)^{D/\alpha} F(t)^{D/2\alpha} \right].$$

The time-dependent part of the exponent is given by:

$$F(t)^{D/2\alpha} = \left[ \int_{-\infty}^{\infty} \int_{-\infty}^{\infty} d\tau d\tau' \lambda(\tau) \lambda(\tau') \langle S^z(\tau) S^z(\tau') \rangle \right]^{D/2\alpha}.$$

Repeating the analysis we did before, considering  $\langle S^z(\tau) S^z(\tau') \rangle = \langle S^2 \rangle e^{-|\tau - \tau'|/\tau_c}$  and  $N = 1$  we obtain:

$$C(t) = \exp \left[ -\gamma^2 n K \times 2\tau_c \{ t - \tau_c (e^{-t/\tau_c} - 4e^{-t/2\tau_c} + 3) \} \right]$$

with  $K = \langle S^2 \rangle / (\alpha 2^{(2\alpha+D)/2\alpha}) \Gamma(-\frac{D}{2\alpha}) \int d\Omega C^{D/\alpha}$ . This results in:

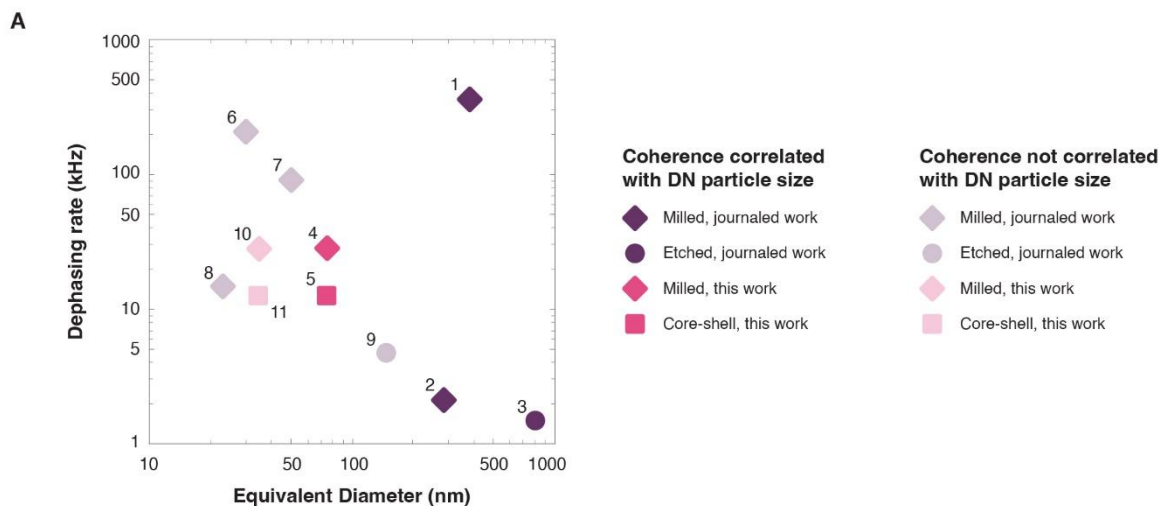
$$C(t) = \begin{cases} \exp \left[ -\gamma^2 n K (t^3/6\tau_c)^{3D/2\alpha} \right], & t \ll \tau_c \\ \exp \left[ -\gamma^2 n K (2t\tau_c)^{3D/2\alpha} \right], & t \gg \tau_c \end{cases},$$

and

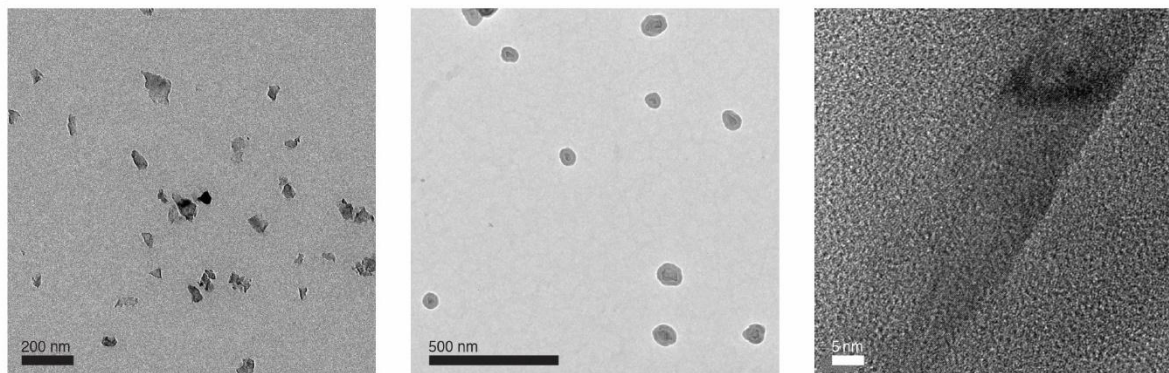
$$\chi(t) \propto \begin{cases} t^{3D/2\alpha}, & t \ll \tau_c \\ t^{D/2\alpha}, & t \gg \tau_c \end{cases}.$$

As can be seen, when considering configurational averaging, the time evolution of the stretching factor has a dependance on the spatial dimensionality of the fluctuators.

## Supporting Information Figures



**Figure S1** – Literature review of dephasing rates vs equivalent particle size. Purple data points indicate literature values and red points indicate the results from this work. Milled diamond nanocrystals (DN) are indicated by diamonds, lithographically fabricated DNs are indicated by circles, and core-shell particles are indicated by square. Opaque colored data points represent measurements where particle size and coherence data were correlated. Faded colored data points indicate values without size correlation. Notably, we found that without size correlation measurements are typically subject to a selection bias for larger particles. This emphasizes the importance of direct size data when comparing studies and experimental conditions. All data points report the longest observed coherence times in a given sample. The numbers refer to references: [1] Ref-2 (28); [2] Ref-3 (29); [3] Ref-4 (30); [4] This work bare nanodiamonds (correlated); [5] This work core-shell nanodiamonds (correlated); [6] Ref-5 (31); [7] Ref-6 (32); [8] Ref-7 (33); [9] Ref-8 (34); [10] This work bare nanodiamonds (average size); [11] This work core-shell nanodiamonds (average size).

**A****B**

**Figure S2 — Growth of silica shell on diamond nanocrystals (A)** Two-step shell growth process including a PVP stabilization step and a sol-gel growth step. The enlarged circle to the right illustrates the expected amorphous silica structure containing alcohols and ethyl groups. **(B)** TEM images of bare (left panel) and core-shell (middle panel) particles. A high-magnification image (right panel) of a DNC encapsulated in silica featuring the diamond crystal lattice lines. Detailed protocol for shell growth can be found in SI1.

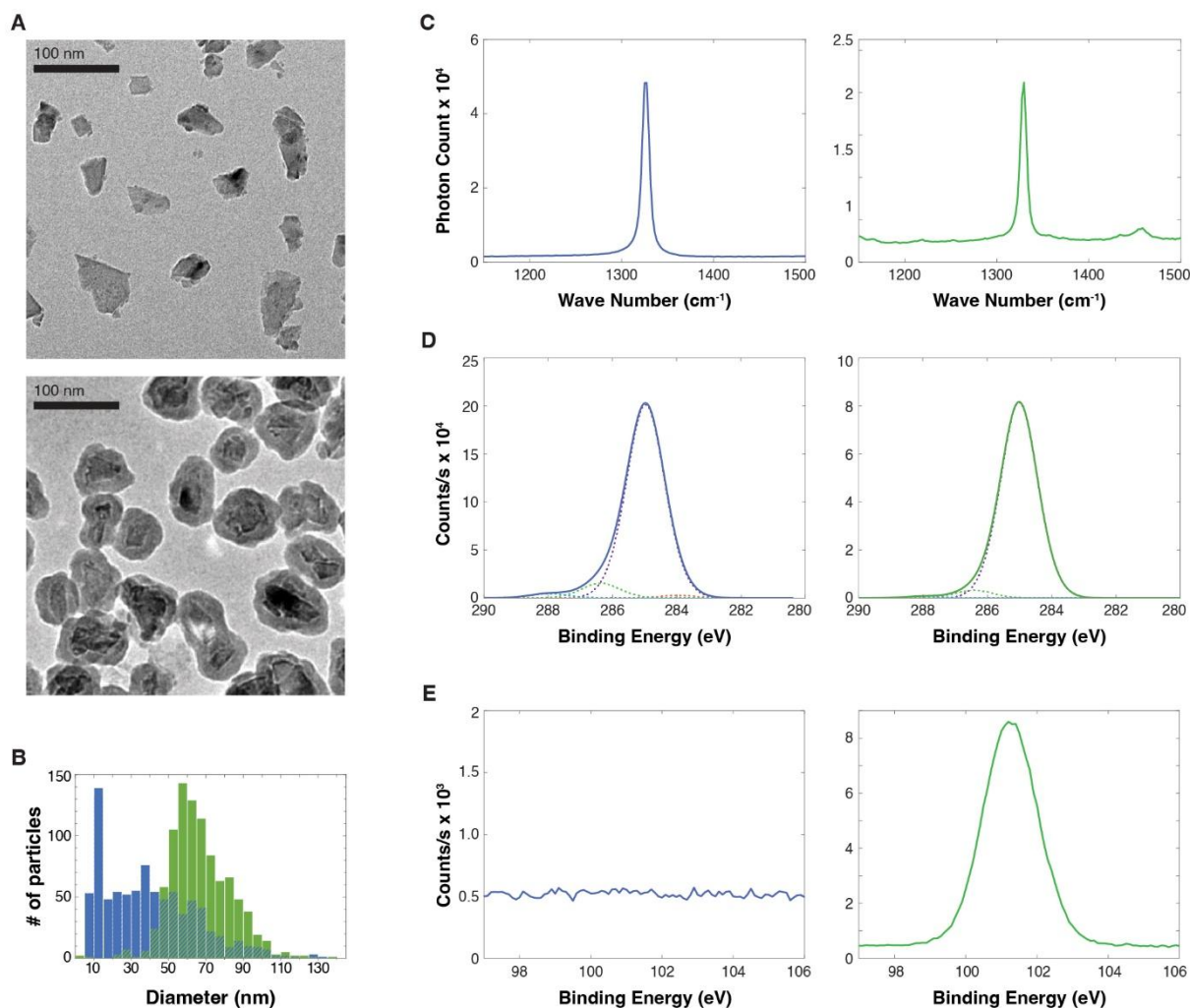


**Figure S3 — Characterization of bare and core-shell diamond nanocrystals. (A)** Original TEM images for Fig. 1A. **(B)** Size distributions obtained from TEM images of bare (blue,  $mean = 39.64 \pm 25.01$  nm,  $N = 855$ ) and core-shell (green,  $mean = 66.88 \pm 16.32$  nm,  $N = 855$ ) particles. **(C)** Raman spectra of bare (left panel) and core-shell (right panel) particles taken at 325 nm and featuring a diamond peak at  $1332 \text{ cm}^{-1}$  with FWHM of  $9.60 \text{ cm}^{-1}$  and  $7.44 \text{ cm}^{-1}$ , respectively. We attribute the feature at  $\sim 1460 \text{ cm}^{-1}$  to carbon chains, as those found in organic compounds or polymers. Specifically, we believe this feature might be related to PVP used during the coating process or other contaminants. **(D)** XPS spectra of bare (left panel) and core-shell (right panel) particles featuring a diamond peak at  $\sim 285$  eV. Dashed curves represent a deconvolution of the peaks to sp<sup>3</sup> (purple at 285 eV; 95.41% for core-shell and 89.88% for bare), C=O (light blue at 288 eV; 0.86% for core-shell and 2.05% for bare), C–O (light green at 286.4 eV; 3.73% for core-shell and 6.86% for bare), and sp<sup>2</sup> (orange at 284 eV; 0% for core-shell and 1.2% for bare). The 30% increase in C–O to C=O ratio and the complete suppression of sp<sup>2</sup> signal in core-shell compared to bare particles may point out to the hydroxylation processes that remove surface mid-gap states. **(E)** XPS spectra of bare (left panel) and core-shell (right panel) particles featuring silica peak at  $\sim 101$  eV.

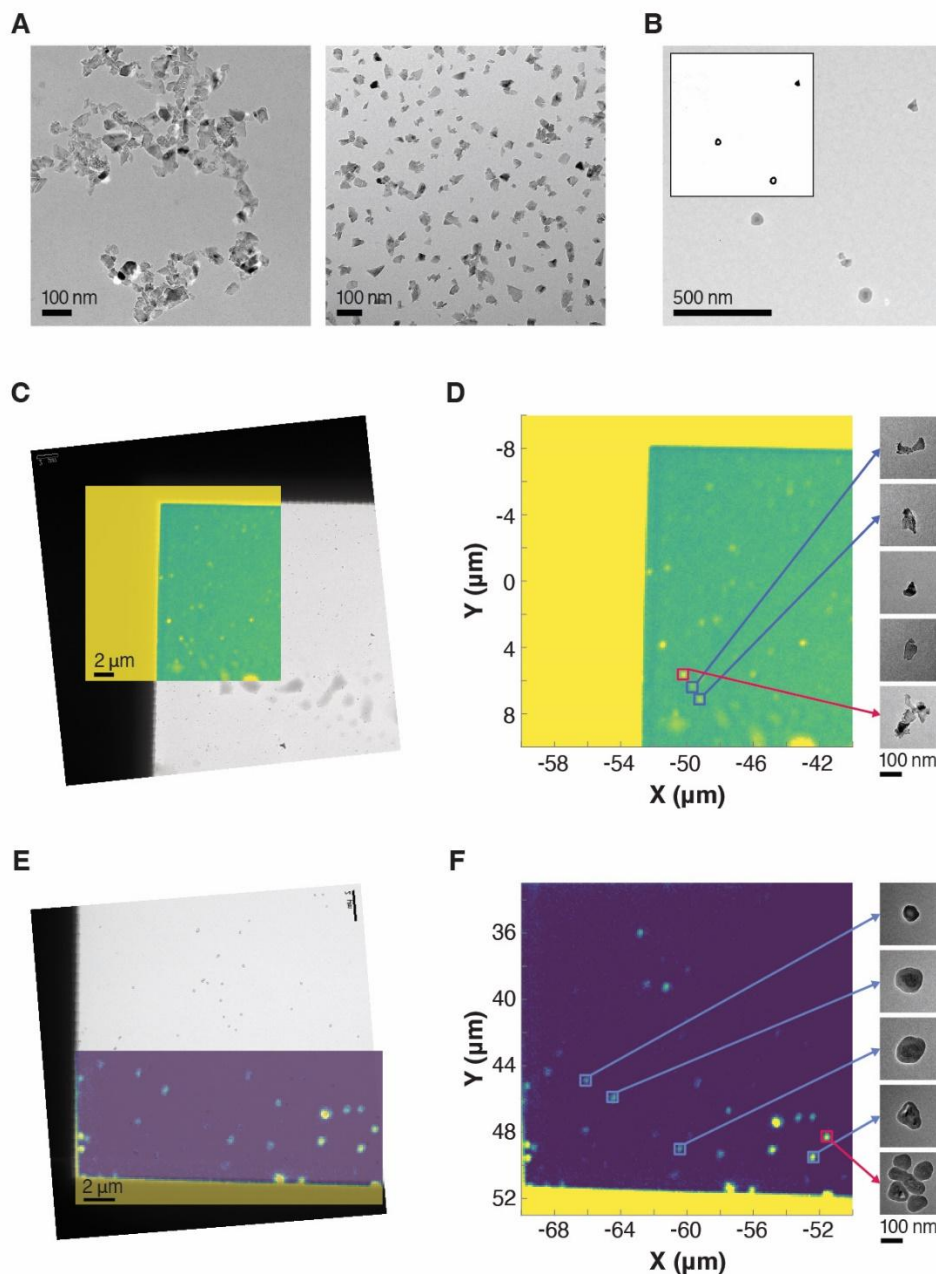


**Figure S4 — TEM grid processing for CLEM and software size analysis.** (A) TEM image of -bare particles deposited on a UV-ozone treated grid (left panel) and a UV-ozone + PEI treated grid (right panel). (B) TEM image of bare and core-shell particles on the same grid. Inset shows the binary image produced after processing and thresholding for area calculations. Only fluorescent particles were processed. (C) Alignment of TEM and confocal image for CLEM of bare particles used in Figure 3C. (D) Enlarged confocal image containing two bare particles that were used in Figure 3 (cyan) and one measurement that was disqualified after classification as an aggregate (red). Note that the other two particles used for  $T_1$  measurements in Figure 3C are found on a separate confocal scan, which is featured in the upper panel of Figure 3D. TEM images of individual particles are shown in the panels to the right. (E) Alignment of TEM and confocal image for CLEM of core-shell particles used in Figure 3C. (F) Enlarged confocal image containing all the core-shell particles that were used for  $T_2$  measurements in Figure 3C (cyan), including one measurement that was disqualified after classification as an aggregate (red). TEM images of individual particles are shown in the panels to the right.

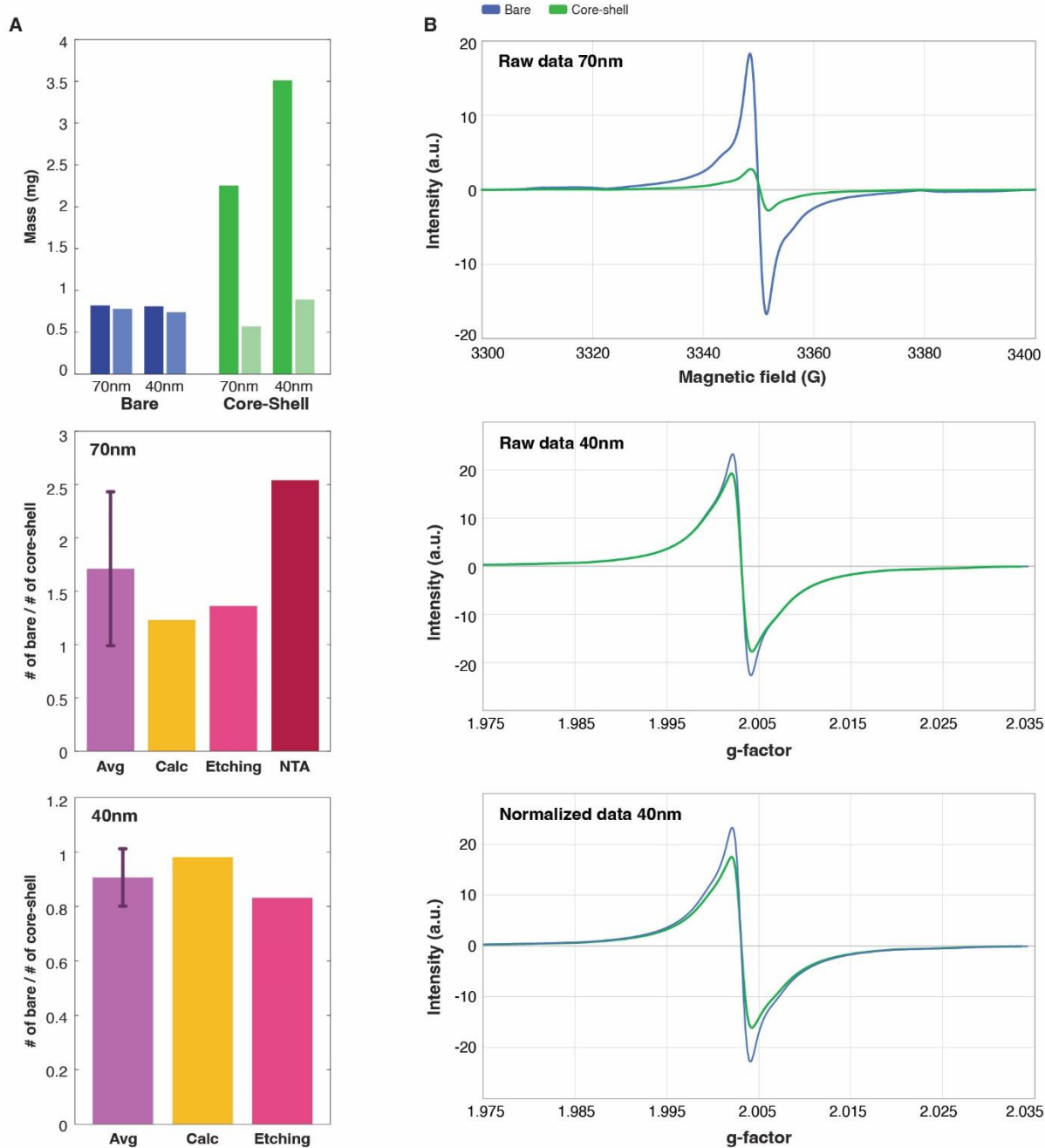


**Figure S5 — EPR of bare and core-shell particles. (A)** Normalization of EPR signals. The upper panel shows the mass of bare (blue) and core-shell (green) 70 and 40 nm particles before (dark shades) and after (light shades) etching with KOH. The lower two panels show all normalization factors,  $F = N_{bare}/N_{CS}$  for 70 nm (middle panel) and 40 nm (lower panel) particles (see SI5 for a detailed description of the normalization procedure). **(B)** Additional EPR data for bare (blue) and core-shell (green) particles. The upper panel shows raw EPR signals for 70 nm particles before normalization (see Fig. 2A, B for the normalized signal). The lower two panels show the raw EPR for 40 nm particles (middle panel) and the normalized signal (lower panel). Resonant frequencies for 70 nm particles were 9.392094 GHz and 9.392505 GHz for bare and core-shell particles, respectively. Resonant frequencies for 40 nm particles were 9.395766 GHz and 9.392509 GHz for bare and core-shell particles, respectively.



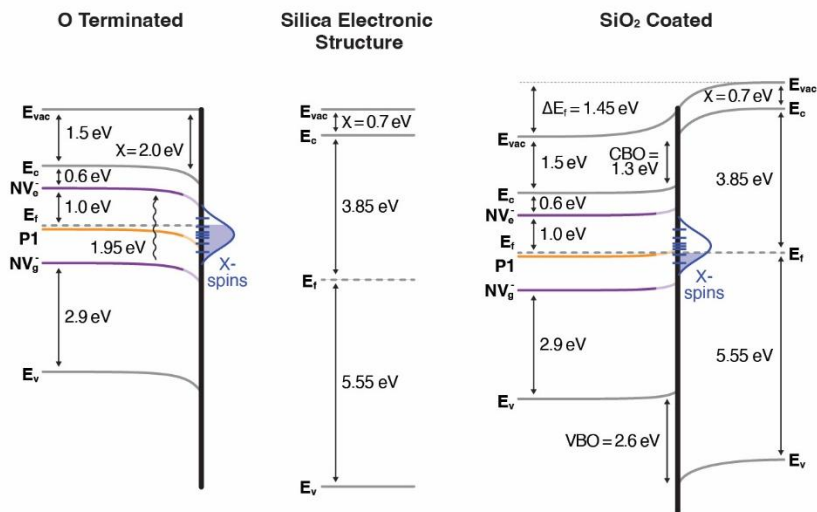


**Figure S6 — Electronic band structures.** The electronic band structure of oxygen-terminated DN (left), amorphous silica (middle), and the heterojunction of the core-shell particles (right), leading to the depletion of paramagnetic P1 (orange line) and X-spins (blue gaussian) after encapsulation in a silica shell. The modeled bending at the diamond interface is  $-0.5$  eV and  $0.225$  eV for bare and core-shell particles, respectively. Our EPR results imply that the X-spins lie near the Fermi level within the diamond band gap. Their location between the NV ground and excited states (purple lines;  $\sim 1.95$  eV gap) implies that these unoccupied states might contribute to NV charge instability during illumination. Previous studies (35–37) point to unoccupied electron states created by carboxylic acids ( $\pi^*C=O$  at 2 eV below the conduction band) as likely candidates to experience a substantial depletion due to the proposed band bending. However, recent reports with boron reduced (38) and silica coated (37) DN reveal that our surface modification depletes surface related  $sp^2$  groups as well, suggesting that the reduction of X-spins reflects a decrease in both types of surface related states. Note that while the illustrated bending in Figure 2C is exaggerated for better visibility, here it is illustrated true to scale.

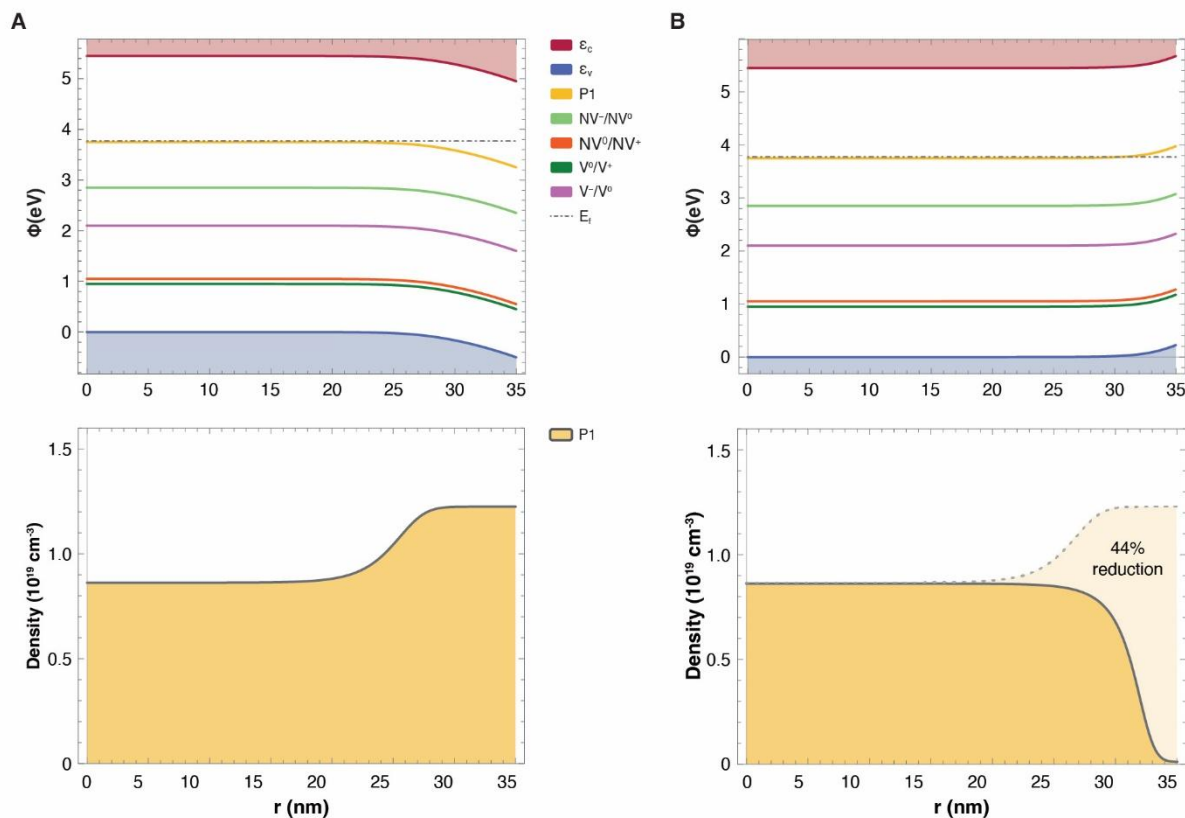


**Figure S7 — Band bending simulation.** (A) Simulation results showing the band diagram (upper panel) and the volumetric density of paramagnetic P1 centers (lower panel) as a function of distance from the center,  $r$ , in a bare DN with oxygen termination. (B) Simulation results showing the band diagram (upper panel) and the volumetric density of paramagnetic P1 centers (lower panel) as a function of  $r$  for core-shell nanocrystal. The expected change in P1 is shown in light gray demonstrating a 44% reduction. See SI6 for simulation details.



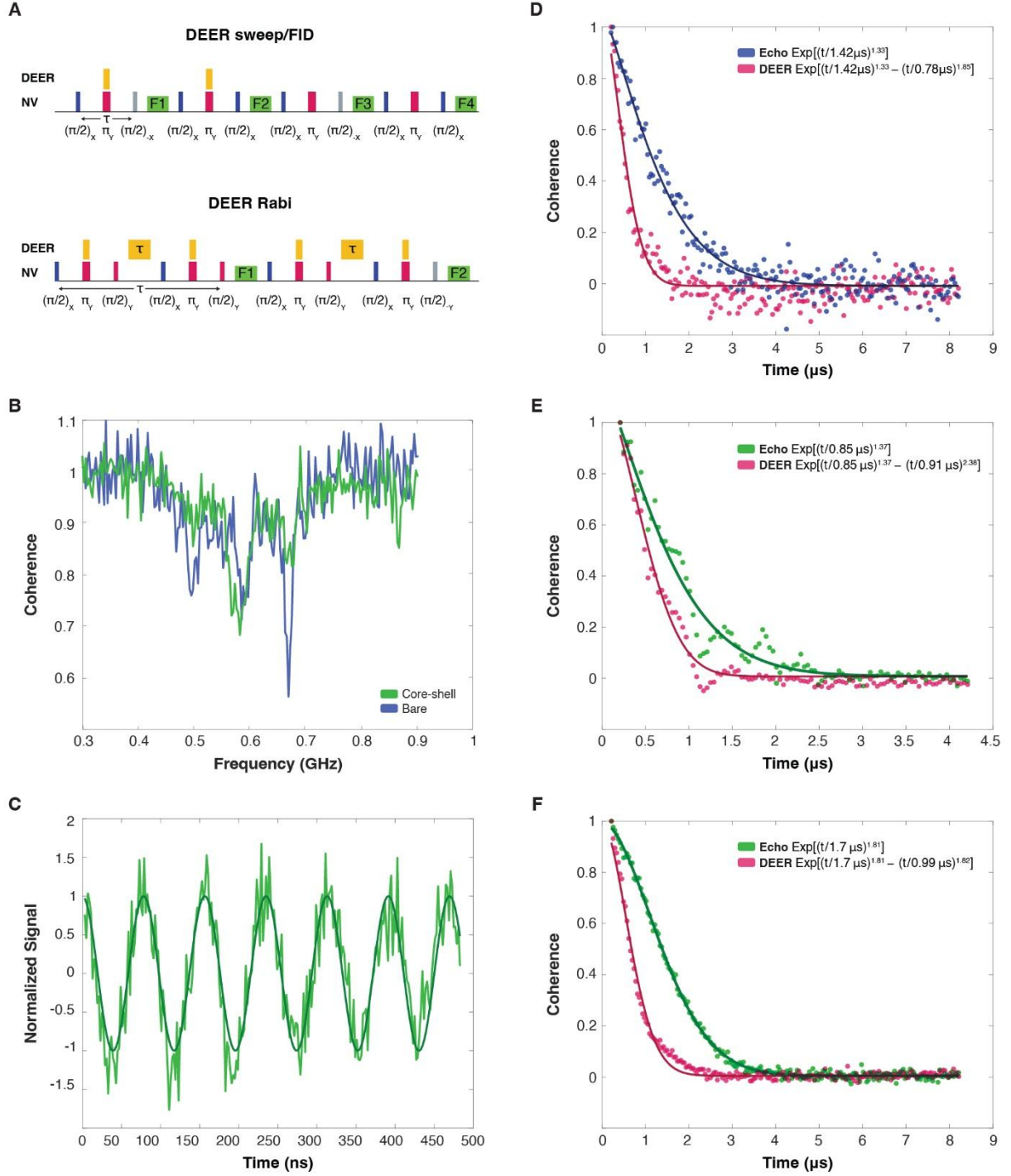


**Figure S8 — DEER measurements.** (A) Sequences used for DEER resonance\FID (top), and DEER Rabi (bottom) measurements. The DEER resonance\FID sequence contains four parts. The first two parts are responsible for DEER decay and end with a  $180^\circ$  phase-flipped  $\pi/2$  pulse to cancel common mode noise (e.g., fluorescence decay due to charge instability). The last two parts of the sequence are responsible for the NV Hahn echo. We use the DEER decay signal,  $S_D = (F1 - F2)/(F1 + F2)$ , and the Hahn-Echo decay signal,  $S_E = (F3 - F4)/(F3 + F4)$  to extract the DEER FID signal defined as:  $S_{FID} = S_D/S_E$ . To find the DEER resonance, we fixed  $t = 400\text{ns}$ , while sweeping the microwave frequency. To extract the FID time trace, we set the microwave frequency to the resonance of the paramagnetic defects,

while sweeping  $t$ . The duration of the  $\pi$  pulse is determined by extracting the DEER Rabi frequency. In the Rabi measurement, we fix  $t$ , while sweeping the duration of the middle DEER pulse. The signal is defined as  $S_{Rabi} = (F1 - F2)/(F1 + F2)$ . The final NV  $\pi/2$  pulse is phase flipped to cancel common mode noise. **(B)** Detected DEER resonances for bare (blue) and core-shell (green) particles at  $\sim 0.498$  GHz,  $\sim 0.591$  GHz, and  $\sim 0.669$  GHz, corresponding to expected values for P1 centers and X-spins. **(C)** DEER Rabi in a core-shell particle confirms coherent driving of paramagnetic defects at 12.8 MHz **(D)** Spin echo (blue) and DEER FID (red) of a bare particle. Inset showing fit results with DEER FID of  $0.78 \mu s$ . (E-F) Spin echo (green) and DEER FID (red) of core-shell particles. Inset showing fit results with DEER FID of  $0.99 \mu s$  **(E)** and  $0.91 \mu s$  **(F)**. The particle in panel **(E)** presents nuclear spin oscillations likely resulting in shorter spin echo time. All measurements were performed at  $\sim 205$  G. See SI7 for more details.

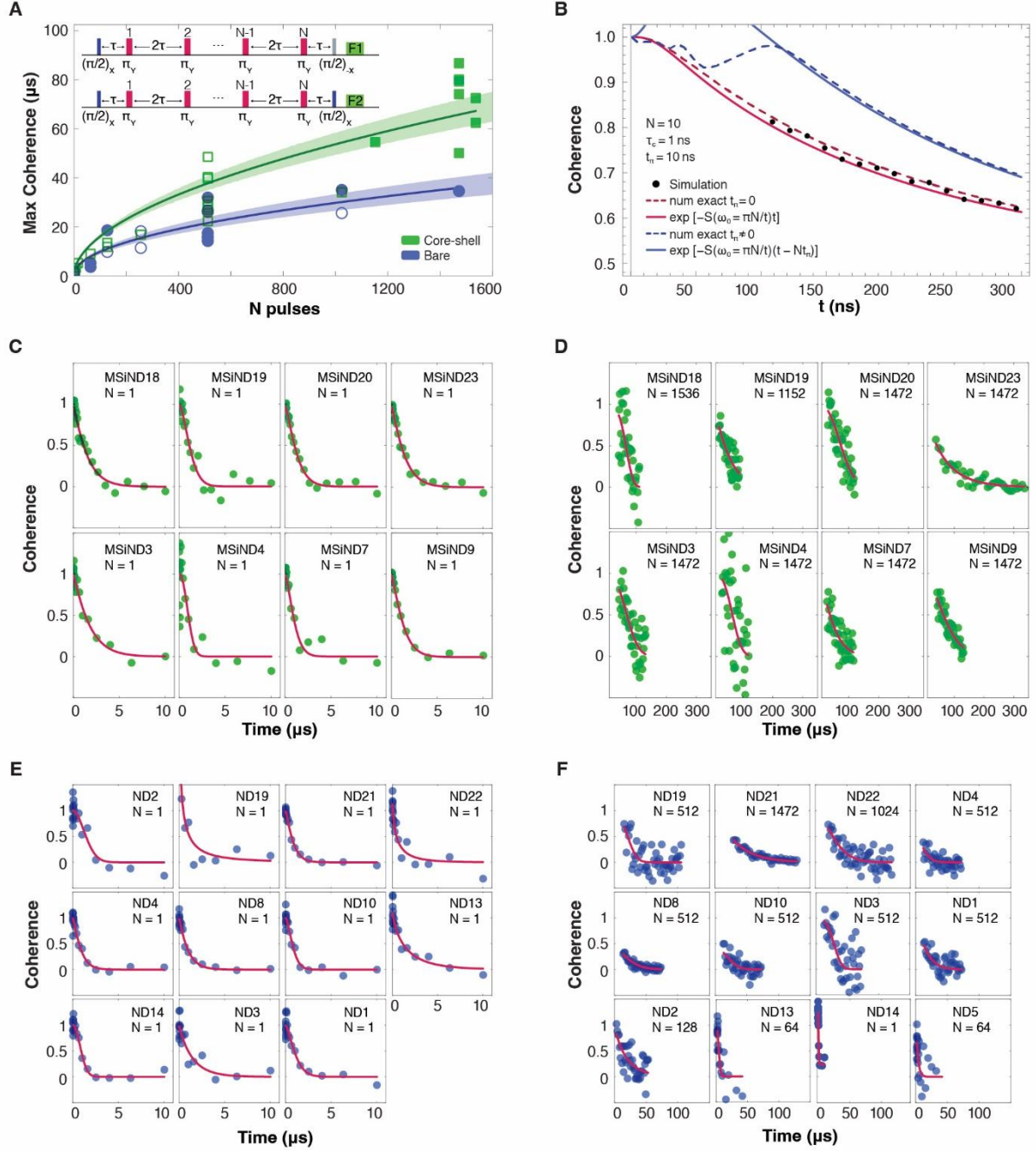


**Figure S9 — T2 measurements.** (A) A full version of Figure 3B featuring all CPMG measurements for bare (blue) and core-shell (green) particles. Fully colored markers represent the maximum T2 measured for a given particle. Solid lines are fits to  $T_2(N) = T_{2,\text{echo}} N^k$ , considering all measurements for a given group. Since all core-shell particles showed measurable improvement for the highest number of pulses measured ( $N > 1000$ ), the fitted parameter  $k = 0.53$  is a representation of the average core-shell particle. Only 2 bare particles continued to show improvement for  $N > 1000$ , and most saturated at a much smaller number of pulses. Therefore, the fitted parameter  $k = 0.47$  represents a higher bound for bare particles that showed a large distribution of  $k = 0$  to  $0.47$ . The sequence used for CPMG measurements is shown in the inset (initialization pulse was ignored). The T2 decay signal was recorded as  $S_{\text{CPMG}} = (F1 - F2)/(F1 + F2)$  and fitted to the time-dependent coherence,  $C(t) = ae^{-\chi(t)}$ , where we defined  $\chi(t) = (\frac{t}{T_2})^n$ .

**(B)** Monte Carlo simulation, assessing the effect of dephasing during the  $\pi$ -pulses. We set  $N = 10$ ,  $\tau_c = 1 \text{ ns}$ , and  $t_\pi = 10 \text{ ns}$  to represent the scenarios in our CPMG measurements where  $\tau_c \leq t_\pi$  and  $Nt_\pi$  is on the same order of magnitude as  $T_2$  (see SI9 for more simulation details). The exact numerical (dashed curves) and the  $C(t) \approx \exp[-S(\omega_0)t]$  approximated (solid curves) coherence signals were calculated assuming no dephasing during the pulse duration (blue) and for an infinitesimally short pulse,  $t_\pi = 0 \text{ ns}$  (red). **(C)** T2 echo signals for the eight measured core-shell particles, with an average  $T_2^{Echo} = 1.42 \pm 0.20 \text{ } \mu\text{s}$ . **(D)** T2 CPMG signals for the eight measured core-shell particles. **(E)** T2 echo signals for eleven measured bare particles (ND5 Echo  $T_2$  wasn't recorded due to an error), with an average  $T_2^{Echo} = 1.05 \pm 0.41 \text{ } \mu\text{s}$ . **(F)** T2 CPMG signals for the twelve measured bare particles.

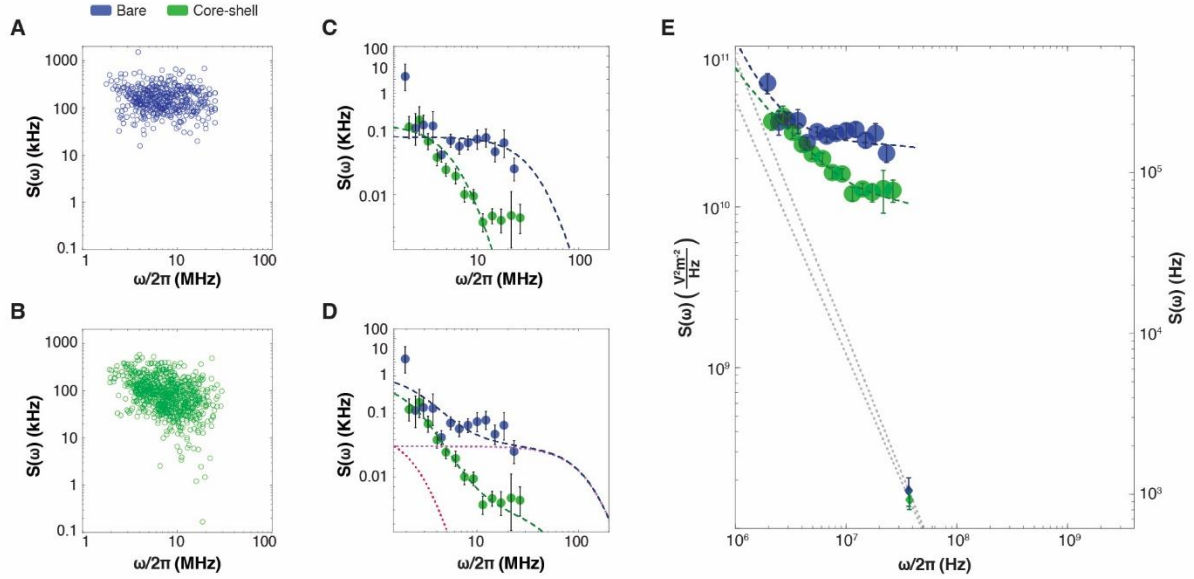


**Figure S10 — Noise spectrum fitting.** All points obtained with the noise spectral density extraction procedure for bare (A) and core-shell (B) particles before binning. (C) The data was grouped into 14 logarithmic bins. A single Lorentzian fit to equation (1) did not fit well for both groups (bare:  $\Delta = 1.4e7$ ,  $\tau_c = 3$  ns,  $rsquare = 0.06$ ; core-shell:  $\Delta = 6.1e6$ ,  $\tau_c = 17$  ns,  $rsquare = 0.63$ ). (D) A double Lorentzian fit described well only the core-shell group (bare:  $\Delta_1 = 3.4e6$ ,  $\tau_{c1} = 44$  ns,  $\Delta_2 = 2.2e7$ ,  $\tau_{c2} = 0.9$  ns,  $rsquare = 0.53$ ; core-shell:  $\Delta_1 = 3.8e6$ ,  $\tau_{c1} = 46$  ns,  $\Delta_2 = 1.1e7$ ,  $\tau_{c2} = 1.7$  ns,  $rsquare = 0.96$ ). Magenta and red dashed lines represent the bare particles' fit for the Lorentzians with short and long  $\tau_c$ , respectively. It is clear that the short  $\tau_c$  Lorentzian is dominant, and that a good fit can only be obtained by adding a Lorentzian with much longer  $\tau_c$ , in the regime dominated by electric noise. (E) fits for both groups were obtained by considering electric field noise and fitting  $1/f$ -like noise using the DQ relaxation data and equation (2). (bare:  $\Delta = 2.4e7$ ,  $\tau_c \leq 1$  ns,  $a = 1.7$ ,  $rsquare = 0.75$ ; core-shell:  $\Delta_{c,1} = 2.9e6$ ,  $\tau_{c,1} = 40$  ns,  $\Delta_{c,2} = 1.3e7$ ,  $\tau_{c,2} \leq 1$  ns,  $a = 1.6$ ,  $rsquare = 0.95$ ). The fitted  $a$  is within the expected range,  $1 \leq a \leq 2$ , arising from one or more Lorentzian noise baths, and agrees well with previous reports (16). All dashed black lines are the fits to the total data. Only CPMG data for pulse number  $N > 64$  was considered to uphold the approximation of the filtering function as a delta function (SI9)

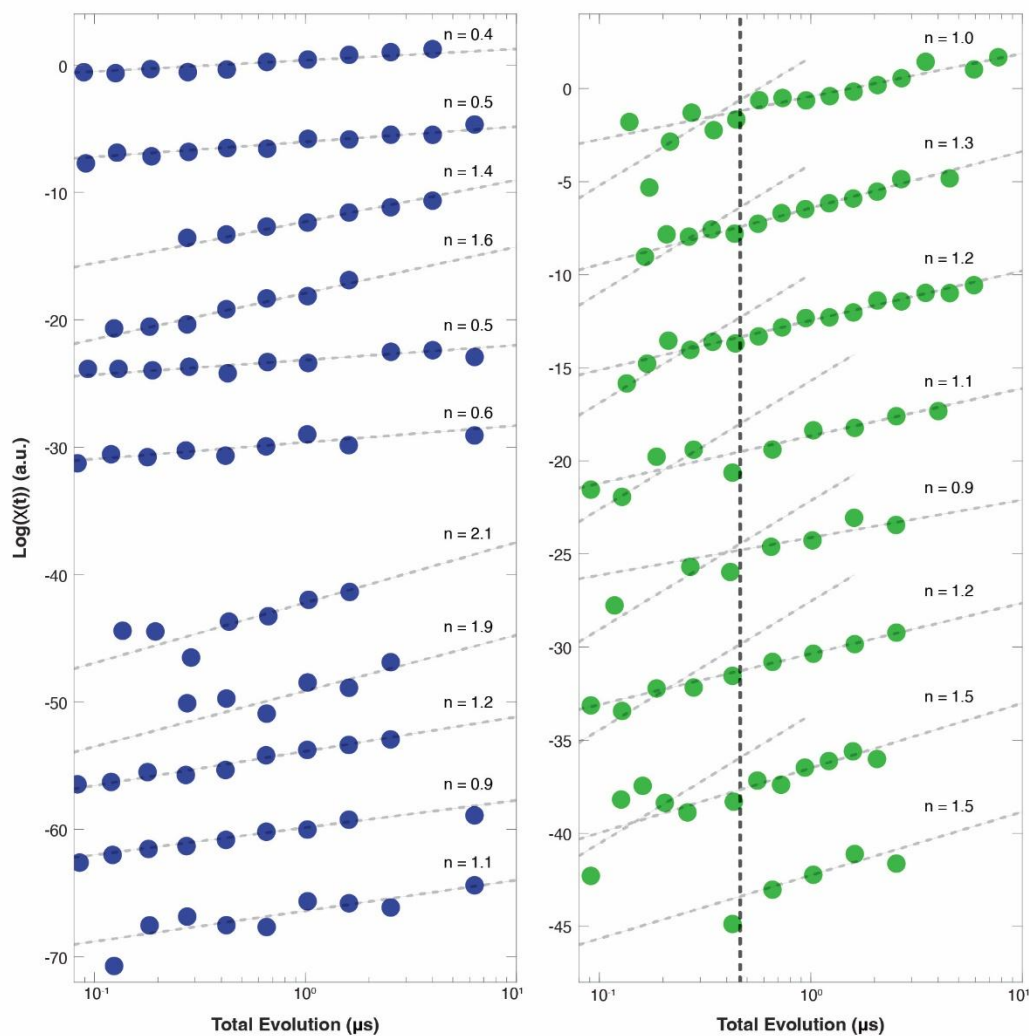


**Figure S11 — Echo stretch factors.** All bare (left panel) and core-shell (right panel) echo stretching factors were extracted as described in Figure 4C. Gray dashed lines are exponential fits for the random walk regime (the cutoff is marked by the black dashed line). For bare particles, the cutoff is too short to plot (30 ns). Core-shell particles also show ballistic regime fits to  $n = 3$  to guide the eye (see methods and SI11 for more details about cutoff choice and plotting procedure).

## SI References

1. W. Stöber, A. Fink, E. Bohn, Controlled growth of monodisperse silica spheres in the micron size range. *J. Colloid Interface Sci.* **26**, 62–69 (1968).
2. C. Graf, D. L. J. Vossen, A. Imhof, A. van Blaaderen, A general method to coat colloidal particles with silica. *Langmuir* **19**, 6693–6700 (2003).
3. I. Rehor, *et al.*, Fluorescent nanodiamonds embedded in biocompatible translucent shells. *Small* **10**, 1106–1115 (2014).
4. I. Rehor, P. Cigler, Precise estimation of HPHT nanodiamond size distribution based on transmission electron microscopy image analysis. *Diam. Relat. Mater.* **46**, 21–24 (2014).
5. E. Janitz, *et al.*, Diamond surface engineering for molecular sensing with nitrogen-vacancy centers. *J. Mater. Chem.* **10**, 13533–13569 (2022).
6. V. Petráková, *et al.*, Luminescence of nanodiamond driven by atomic functionalization: Towards novel detection principles. *Adv. Funct. Mater.* **22**, 812–819 (2012).
7. N. W. Ashcroft, N. David Mermin, *Solid State Physics* (Holt, Rinehart and Winston, 1976).
8. D. A. Broadway, *et al.*, Spatial mapping of band bending in semiconductor devices using in situ quantum sensors. *Nature Electronics* **1**, 502–507 (2018).
9. P. Deák, B. Aradi, M. Kaviani, T. Frauenheim, A. Gali, Formation of NV centers in diamond: A theoretical study based on calculated transitions and migration of nitrogen and vacancy related defects. *Phys. Rev. B Condens. Matter* **89**, 075203 (2014).
10. O. A. Shenderova, *et al.*, Review Article: Synthesis, properties, and applications of fluorescent diamond particles. *J. Vac. Sci. Technol. B Nanotechnol. Microelectron.* **37**, 030802 (2019).
11. N. Nunn, *et al.*, Electron irradiation-induced paramagnetic and fluorescent defects in type Ib high pressure–high temperature microcrystalline diamonds and their evolution upon annealing. *J. Appl. Phys.* **132**, 075106 (2022).
12. S. Sangtawesin, *et al.*, Origins of Diamond Surface Noise Probed by Correlating Single-Spin Measurements with Surface Spectroscopy. *Phys. Rev. X* **9**, 031052 (2019).
13. B. L. Dwyer, *et al.*, Probing Spin Dynamics on Diamond Surfaces Using a Single Quantum Sensor. *PRX Quantum* **3**, 040328 (2022).
14. J. D. A. Wood, *et al.*, Wide-band nanoscale magnetic resonance spectroscopy using quantum relaxation of a single spin in diamond. *Phys. Rev. B Condens. Matter* **94**, 155402 (2016).
15. M. J. Biercuk, *et al.*, Optimized dynamical decoupling in a model quantum memory. *Nature* **458**, 996–1000 (2009).
16. B. A. Myers, A. Ariyaratne, A. C. B. Jayich, Double-Quantum Spin-Relaxation Limits to Coherence of Near-Surface Nitrogen-Vacancy Centers. *Phys. Rev. Lett.* **118**, 197201 (2017).
17. D. R. Candido, M. E. Flatté, Interplay between charge and spin noise in the near-surface theory of decoherence and relaxation of C3v symmetry qutrit spin-1 centers. *Phys. Rev. B.* **110**, 024419 (2024).
18. T. Rosskopf, *et al.*, Investigation of surface magnetic noise by shallow spins in diamond. *Phys. Rev. Lett.* **112**, 147602 (2014).

19. B. A. Myers, *et al.*, Probing surface noise with depth-calibrated spins in diamond. *Phys. Rev. Lett.* **113**, 027602 (2014).
20. C. A. Meriles, *et al.*, Imaging mesoscopic nuclear spin noise with a diamond magnetometer. *J. Chem. Phys.* **133**, 124105 (2010).
21. G. S. Uhrig, Keeping a quantum bit alive by optimized pi-pulse sequences. *Phys. Rev. Lett.* **98**, 100504 (2007).
22. W. Yang, W.-L. Ma, R.-B. Liu, Quantum many-body theory for electron spin decoherence in nanoscale nuclear spin baths. *Rep. Prog. Phys.* **80**, 016001 (2017).
23. E. J. Davis, *et al.*, Probing many-body dynamics in a two-dimensional dipolar spin ensemble. *Nat. Phys.* **19**, 836–844 (2023).
24. E. B. Fel'dman, S. Lacelle, Configurational averaging of dipolar interactions in magnetically diluted spin networks. *J. Chem. Phys.* **104**, 2000–2009 (1996).
25. J. R. Klauder, P. W. Anderson, Spectral Diffusion Decay in Spin Resonance Experiments. *Phys. Rev.* **125**, 912–932 (1962).
26. R. Mukherjee, T. C. Killian, K. R. A. Hazzard, Accessing Rydberg-dressed interactions using many-body Ramsey dynamics. *Phys. Rev. A* **94**, 053422 (2016).
27. P. Schultzen, *et al.*, Glassy quantum dynamics of disordered Ising spins. *Phys. Rev. B Condens. Matter* **105**, L020201 (2022).
28. K. Oshimi, *et al.*, Bright quantum-grade fluorescent nanodiamonds. *ACS Nano* **18**, 35202–35213 (2024).
29. B. D. Wood, *et al.*, Long spin coherence times of nitrogen vacancy centers in milled nanodiamonds. *Phys. Rev. B* **105** (2022).
30. P. Andrich, *et al.*, Engineered micro- and nanoscale diamonds as mobile probes for high-resolution sensing in fluid. *Nano Lett.* **14**, 4959–4964 (2014).
31. B. Naydenov, *et al.*, Dynamical decoupling of a single-electron spin at room temperature. *Phys. Rev. B Condens. Matter Mater. Phys.* **83** (2011).
32. A. Laraoui, J. S. Hodges, C. A. Meriles, Nitrogen-vacancy-assisted magnetometry of paramagnetic centers in an individual diamond nanocrystal. *Nano Lett.* **12**, 3477–3482 (2012).
33. H. S. Knowles, D. M. Kara, M. Atatüre, Observing bulk diamond spin coherence in high-purity nanodiamonds. *Nat. Mater.* **13**, 21–25 (2014).
34. M. E. Trusheim, *et al.*, Scalable fabrication of high purity diamond nanocrystals with long-spin-coherence nitrogen vacancy centers. *Nano Lett.* **14**, 32–36 (2014).
35. A. Wolcott, *et al.*, Surface structure of aerobically oxidized Diamond nanocrystals. *J. Phys. Chem. C Nanomater. Interfaces* **118**, 26695–26702 (2014).
36. A. Chemin, *et al.*, Surface-mediated charge transfer of photogenerated carriers in Diamond. *Small Methods* **7**, e2300423 (2023).
37. P. J. Sandoval, *et al.*, Quantum diamonds at the beach: Chemical insights into silica growth on nanoscale Diamond using multimodal characterization and Simulation. *ACS Nanosci. Au* **3**, 462–474 (2023).



38. R. G. Ryan, *et al.*, Impact of Surface Functionalization on the Quantum Coherence of Nitrogen-Vacancy Centers in Nanodiamonds. *ACS Appl. Mater. Interfaces* **10**, 13143–13149 (2018).